PAPER

Check for updates

Insights into the plasmonic "hot spots" and efficient hot electron injection induced by Ag nanoparticles in a covalent organic framework for photocatalytic H₂ evolution†

Lihua Zhang,[ab] Xu Lu,[a] Jiaqi Sun,[ab] Cunxia Wang[ab] and Pengyu Dong 🔟 *[a]

The effective utilization of the local surface plasmon resonance (LSPR) effect of metal nanoparticles to improve optical absorption capacity and inject hot electrons into photocatalysts opens up new directions and ideas to solve the problem of solar energy utilization efficiency of photocatalysts. In this study, we created an *in situ* technique for preparing plasmon Ag nanoparticles (NPs) decorated with a covalent organic framework (COF), named Ag/TpPa-1-COF. The LSPR effect of Ag NPs results in an outstanding rate of H₂ production that is 801.4 µmol g^{-1} h^{-1} for the 3% Ag/TpPa-1 photocatalyst, which is almost 4 times as effective as that of the unmodified TpPa-1-COF. Moreover, finite-difference time-domain (FDTD) simulation results reveal that the strongest electric field intensity is presented when the catalyst is excited at $\lambda = 465$ nm. Furthermore, plasmonic "hot spots" induced by the interfacial electric field enhancement factor distribution of Ag/TpPa-1 were simulated in detail by adjusting the number, particle size, and gap distance of Ag NPs. Additionally, density functional theory (DFT) calculations show that electron transfer from Ag NPs to TpPa-1 occurs at the Ag/TpPa-1 interface, and N sites in Ag/TpPa-1 exhibit low Gibbs free energy (ΔG_{H*}) for enhanced photocatalytic H₂ evolution. Overall, this research provides new insights into the plasmonic "hot spot" region that performs effectively for hydrogen evolution.

1. Introduction

In the past several decades, owing to the growing demand for clean energy, efficient and environmentally conscious hydrogen manufacturing processes have attracted considerable attention.[1,2] Among various approaches, employing sunlight to power a process that splits water into hydrogen and oxygen (photocatalysis) has been considered a vital direction for future energy development.[3–6] The creation of photocatalysts that can efficiently capture broad solar light is a crucial component of photocatalytic hydrogen evolution.[7–9]

Covalent organic frameworks (COFs) are a type of porous crystalline substances made up of organic molecules linked together *via* covalent bonds, which show excellent application prospects in photocatalytic hydrogen research.[10–14] TpPa-1-COF is considered to be a typical material of COFs linked *via* β-ketoenamine with 2D structural characteristics, wide light harvesting characteristics in the optimal visible range, and are an extremely suitable photocatalyst being applied in water splitting.[15,16] For instance, Shi's research group loaded TiO₂ nanosheets on TpPa-1-COF to prepare heterogeneous composite materials with high hydrogen production performance.[17] Zhang's research group developed two types of heterostructures of NH₂-UiO-66/TpPa-1 covalently linked *via* Z-type heterojunctions and TiO₂-TpPa-1-COF without noble metals,[18,19] and rationally introduced electron-donating groups (*e.g.* –H, –(CH₃)₂, and –NO₂) to TpPa-1-COF to obtain high photocatalytic hydrogen evolution.[20] In addition, previous works by Dong *et al.* demonstrated that extremely chemically stable TpPa-1-COF could be used to anchor Pt single atoms,[21] embed [Mo₃S₁₃]²⁻ nanoclusters into their micropores,[22] and hybridize an S-scheme heterojunction with ZnIn₂S₄ (ref. 23) and g-C₃N₄ nanosheets.[24] These studies demonstrated that the photogenerated carrier dynamics of TpPa-1-COF could be regulated by constructing heterogeneous composite materials or heterojunctions to boost photocatalytic H₂ evolution performance.

Because of their distinctive localized surface plasmon resonance (LSPR) effect, the improvement in photocatalytic

[a]Key Laboratory for Advanced Technology in Environmental Protection of Jiangsu Province, Yancheng Institute of Technology, Yancheng 224051, P. R. China. E-mail: dongpy11@gmail.com

[b]School of Mechanical Engineering, Yancheng Institute of Technology, Yancheng 224051, P. R. China

† Electronic supplementary information (ESI) available: SEM images; TEM images; the standard curve of H₂ production; the chromatogram of H₂ evolved over TpPa-1-COF; the chromatogram of H₂ evolved over 3% Ag/TpPa-1; a comparison of XRD pattern, FTIR spectrum, XPS spectrum, and TEM image of 3% Ag/TpPa-1 before and after photocatalysis; the constructed geometry model; H₂ evolution process; summary of H₂ evolution activity of some COFs-based photocatalytic systems. See DOI: https://doi.org/10.1039/d3ta06724f

5392 | *J. Mater. Chem. A*, 2024, **12**, 5392–5405

This journal is © The Royal Society of Chemistry 2024

efficiency induced by noble metals is a current research hotspot in the field of energy.[25–28] In the LSPR mode, free electrons in metal nanocrystals bounce collectively under resonant stimulation. In addition to giving metal nanocrystals enormous absorption cross-sections, it may also produce hot electrons or high-energy photogenerated electrons.[29,30] Moreover, the shape, content, and size of the plasmonic nanoparticles (NPs) have a major role in the light-harvesting range and near-field dispersion of LSPR effect.[31] More intriguingly, the "hot spots" are regions where the plasmon-enhanced field is especially large, usually appearing in the tip, corner, and edge of a plasmonic metal nanoparticle, or the fissure between two (or more) particles.[32,33] These regions are frequently where the spatially averaged enhancement factor is dominant. Besides, the plasmonic metal (Au, Ag, or Cu) nanocrystals in contact with n-type semiconductors can be optimized by aligning their Fermi levels. By absorbing photons, the nonradiative decay of localized surface plasmon can produce high-energy "hot electrons" and subsequently injected into the conduction band of a nearby semiconductor, which is useful for opening up kinetically difficult multielectron reaction routes and lowering activation barriers.[34] Consequently, it effectively segregates electrons from holes at the interface. The characteristics of these systems encompass enhanced absorption of the incident light, a low rate of electron–hole recombination, and improved light energy conversion of the photocatalytic materials. These constructions consist of plasmonic metals and semiconductors.[35,36] Conventional cocatalyst/semiconductor devices have been demonstrated to exhibit enhanced effectiveness.[37] Recently, the construction of heterogeneous photocatalysts using metal nanoparticles and semiconductors has been used in developing high-performing photocatalysts. In all kinds of metals, Ag has substantial quality factor possession, directly correlated with the strength of LSPR, across a broad wavelength range spanning from 300 to 1200 nm.[38,39] Ag NPs could be immobilized on appropriate supports or matrices in order to be used to the fullest extent possible.

Although plasmonic metal-loaded semiconductor photocatalysts have been extensively studied in recent years, there is little research on the plasmonic metal-loaded COF photocatalysts. COFs, as crystalline porous materials with adjustable characteristics, have become promising materials for hosting Ag NPs owing to their significant surface area, chemical resistance, and robust structure. In contrast to earlier research, in this work, plasmonic hot electrons induced by Ag NPs were introduced to regulate the photogenerated carrier dynamics of TpPa-1-COF. Moreover, the migration of Fermi levels between Ag NPs and TpPa-1-COF induces the creation of an electric field resonance through LSPR. Furthermore, utilizing the finite-difference time-domain (FDTD) method, a numerical simulation of the generation of an electric field has been carried out. The FDTD method is a numerical calculation method based on the Maxwell equation, which was widely used in electric field simulation and analysis to obtain the features of the dynamic electromagnetic field.[40] The efficient meshing of complex optical structures could be realized by using the space-time step difference to solve the differential equation. FDTD simulation

could provide information on the mechanism of hot electron generation and "hot spots" modulation resulting from the LSPR effect. Herein, the plasmonic "hot spots" induced by the interfacial electric field intensity distribution of Ag/TpPa-1-COFs were investigated using the FDTD simulation by adjusting the excitation wavelengths, number, particle size, and the gap distance of Ag NPs, which could bring some fresh insights into the plasmonic "hot spots" region and efficient hot electron injection. Additionally, density functional theory (DFT) was used to analyze the energy barrier for the formation of H*. Besides, DFT calculation of the charge differential density of Ag/TpPa-1 could provide a basis for understanding the migration path of hot electrons generated by the Ag NPs' LSPR effect. Combined with FDTD and DFT methods, the hot electron generation, "hot spots" modulation mechanism, and hot electron migration path caused by the LSPR effect of Ag NPs in Ag/TpPa-1 can be accurately analyzed, which provides a theoretical basis for enhancing the generation of hydrogen by photocatalysis in experiments. These outcomes yield valuable insights into the further research comprehension of plasmonic photocatalysis.

2. Experimental section

2.1 The preparation of TpPa-1-COF

With slight changes, the technique for the synthesis of TpPa-1-COF described in the literature was adopted.[41] In the beginning, 869.6 mg (5.0 mmol) of *p*-toluene sulphonic acid (monohydrate, PTSA) was mashed for 5 min with 97.2 mg (0.9 mmol) of *p*-phenylenediamine (Pa-1). After adding 129.8 mg (0.6 mmol) of 1,3,5-triformylphloroglucinol (Tp), the mixture was once again crushed. Subsequently, 100 μL (5.5 mmol) of deionized water was introduced progressively to the mixture described above after grinding for 10 min, and the mixture was then finely powdered for 5 min. It was promptly transferred to a watch glass and heated in a 170 °C oven, where it was kept for 2 min. After the paste had cooled to *ca.* 25 °C, it was centrifuged and cleaned in the following order: *N,N*-dimethylacetamide, distilled water, as well as acetone. After gathering the finished products, they were dried for an entire night at 60 °C to produce bare TpPa-1-COF.

2.2 The preparation of Ag/TpPa-1-COF

In a typical process, a 100 mL vial of 1,2-propyleneglycol (1,2-PG, 5 mL) containing 3 g of poly(vinyl pyrrolidone) (PVP, MW = 40 000) was placed inside, sealed, and heated for one hour at 160 °C in an oil bath with condensation and reflux while being stirred. Then, 1 mL of NaCl solution (1 M in 1,2-PG) was quickly added to the above solution. Subsequently, 50 mg of freshly manufactured pure TpPa-1-COF was introduced to the above solution after 5 minutes. After a duration of 10 minutes, a 0.15 M solution of $AgNO_3$ in 1,2-PG was slowly introduced into the stirring solution. Subsequently, the vial was tightly sealed and heated for 40 minutes at 160 °C. Afterward, the product of the reaction was chilled to ambient temperature. The products were then dried at room temperature after being centrifuged

multiple times to eliminate any remaining polyols and PVP to obtain the Ag/TpPa-1-COF sample. It should be noted that the loading quantities of Ag NPs could be regulated by adjusting the volume of AgNO$_3$ solution in 1,2-PG, which are 31, 93, and 155 µL for Ag/TpPa-1 with nominal Ag NPs loading quantities of 1, 3, and 5 wt%, respectively.

2.3 Characterization

Using Cu–K X-ray photons at a voltage of 40 kV, a powder X-ray diffraction pattern (PXRD) was obtained on a PANalytical X'Pert.[3] At 77 K, N$_2$ adsorption–desorption isotherms were measured using the Micromeritics ASAP 2020 analyzer. The FEI Nova NanoSEM 450 was used to obtain scanning electron microscopy (SEM) images. A JEOL JEM-2100F operating at 200 kV was used to perform transmission electron microscopy (TEM), high-resolution TEM (HRTEM), and high-angle annular dark-field scanning transmission electron microscopy (HAADF-STEM). NICOLET NEXUS-670 was used to acquire FT-IR spectra between 400 and 4000 cm^{-1}. All X-ray photoelectron spectra (XPS) were acquired using a Thermo Fisher Scientific ESCALAB 250Xi with Al K radiation at 1486.6 eV and a 500 µm spot size, with binding energies calibrated using C 1s at 284.8 eV. Ag K-edge extended X-ray absorption fine structure spectra (EXAFS) were captured in high energy mode and performed on the BL11B beamline Shanghai Synchrotron Radiation Facility (SSRF) (Shanghai, China), in which the radiation was monochromatized by a Si (311) crystal monochromator, and the data reduction and analysis of X-ray absorption near-edge structure (XANES) spectra, Fourier transform EXAFS (FT-EXAFS) spectra, and wavelet transform EXAFS (WT-EXAFS) spectra were completed by using Athena and Artemis software. Using a Thermo Fisher iCAP PRO spectrometer, inductively coupled plasma optical emission spectroscopy (ICP-OES) was carried out. The BaSO$_4$ standard was used to acquire UV-Vis diffuse reflectance spectra (DRS) using a Shimadzu Corporation UV-3600 spectrometer. An FLS980 fluorescence spectrometer was used to record both photoluminescent (PL) spectra and time-resolved PL spectra. The CHI 660E electrochemical workstation was used for all the photoelectrochemical (PEC) testing. A typical photocatalyst-coated ITO electrode film was prepared according to the literature.[42]

2.4 Photocatalytic hydrogen evolution measurements

At the beginning, a 20 mg sample was suspended in a 100 mL solution of 0.1 mol L^{-1} ascorbic acid (AC) in a Pyrex reactor equipped with a shutdown gas system and a top-irradiation setup. It should be noted that AC has strong reducing properties, which can effectively trap photogenerated holes and form stable reduction products without causing unexpected oxidation reactions to ensure the photocatalytic hydrogen production reaction is more specific. In addition, AC is relatively stable in aqueous solution and is not easily decomposed by itself, which is very important for the reproducibility and stability of photocatalytic hydrogen production experiments. Therefore, 0.1 mol L^{-1} AC solution was used as the sacrificial reagent in the photocatalytic hydrogen production experiments. The reactor

underwent approximately 1 h of flowing Ar gas to create the desired reaction environment. Visible light irradiation conditions were achieved using a 300 W xenon lamp (CEL-HXF300) fitted with a 420 nm cut-off filter, and the visible light power density was found to be 265 mW cm^{-2}. A cooling circulation system was used to maintain the reaction temperature at 6 °C to remove the heat produced by the light source during the experiment. Ultra-pure Ar was employed as the carrier gas, and the evolved H$_2$ was quantified using gas chromatography (GC-2011, TCD). To assess the long-term performance of the catalyst, stability testing was conducted under identical processing conditions for five cycles, totaling 30 h. Additionally, the experimental configuration was employed to assess the AQE of H$_2$ evolution, allowing for flexibility in modifying the illumination source. This involved using a 300 W xenon lamp with band-pass filters set at wavelengths of 420, 450, 500, 550, and 600 nm to emit monochromatic light with precise wavelength control. Using an optical power meter (Newport 843-R), the monochromatic photon flux at each wavelength was determined. Therefore, the calculation of AQE can be carried out using eqn (1).[43]

$$\mathrm{AQE} = \frac{2 \times \text{ amount of H}_2 \text{ molecules produced per hour}}{\text{number of incident photons per hour}} \times 100\%$$

$$= \frac{2 \times n_{\mathrm{H_2}} \times N_{\mathrm{A}} \times h \times c}{P \times t \times \lambda \times A} \times 100\%$$

$$(1)$$

where $n_{\mathrm{H_2}}$ denotes the number of H$_2$ molecules that have evolved, c signifies the speed of light, h denotes the Planck constant, N_{A} represents the Avogadro constant, and t denotes the time during which the irradiation was applied.

2.5 FDTD simulation

The numerical simulation model of the interfacial electric field intensity distribution of Ag NPs in TpPa-1-COF was performed utilizing the 3D finite element approach with COMSOL Multiphysics 5.6 software. To achieve an accurate description of the simulation system, we discretized the continuous time domain rotation Maxwell equation into the displayed difference equation after setting the appropriate boundary conditions. This process not only preserved the complexity of the optical structure but also provided us with an effective means to efficiently deal with the characteristics of electromagnetic fields in calculations. The simulation model was a cubic shape with equal sides ($a = 1$ µm), in which the model was divided into four parts: the Ag NPs (semisphere with a 20 nm diameter), TpPa-1-COF modeling (dimensions: 1 µm × 1 µm × 50 nm), air layer for calculating the physical results, and the perfect matching layer. To ensure accuracy, the mesh grid precision of 0.001 nm was utilized within the simulation area to represent the model precisely. The refractive indices (n) in the model are $n_{\mathrm{a}} = 1$ for air and $n_{\mathrm{b}} = 1.6$ for TpPa-1-COF. The parameters of Ag NPs and the refractive indices are taken from the "Optical Materials Database". A plane wave source (total field scattered field source) with a wavelength (λ) of 420, 465, and 500 nm was used to illuminate the model.

2.6 DFT calculations

With the periodic boundary conditions present, the Materials Studio Package was used. To study electron exchange and correlation, the Perdew–Burke–Eznerhof (PBE) function of generalized gradient approximation (GGA) was used. A threshold energy of 400 eV was used to determine the computation accuracy. Additionally, using a k-point grid and the Monkhorst–Pack sampling technique, the Brillouin zone was sampled with a resolution of 0.2 Å^{-1}. The bottom layers have a connection to the bulk crystal geometry during the structural relaxations. The geometry was adjusted until the energy and force differences reached 1.0×10^{-6} eV and 0.005 eV Å^{-1}, respectively.

3. Results and discussion

The synthesis of crystalline TpPa-1-COF was achieved using a molecular organization approach through a reversible Schiff base reaction and an irreversible enol-to-keto tautomerization, which makes the product more stable.[15,41] Then, the noble-metal plasmonic photocatalyst Ag/TpPa-1 was created using a simple *in situ* technique, in which the hydrophobic carbon chains in PVP can prevent the aggregation of Ag NPs and stabilize the reaction system because of the strong repulsion (steric hindrance effect) in water.[44] Thus, on the surface of 2D TpPa-1-COF, Ag NPs are deposited. Scheme 1 depicts the multistep synthetic process for the Ag/TpPa-1-COF composite photocatalyst.

3.1 Structural characterization

In Fig. 1a, distinct peaks at 4.8, 8.7, and 26° are observed in all four samples. The peaks observed at 4.8 and 8.7° show the in-plane structural packing model and are assigned to the (100) and (200) crystal planes, respectively. Additionally, TpPa-1-COF exhibits π–π stacking between their layers, as seen by the peak at 26°, which corresponds to the (001) crystal plane.[15] In addition to the TpPa-1-COF characteristic peak, the 3% Ag/TpPa-1 and 5% Ag/TpPa-1 composites display distinct peaks at 38.0, 44.3, 64.5, and 77.5°, which coincide with the (111), (200), (220), and (311) crystal planes of the cubic phase of Ag, respectively.[45]
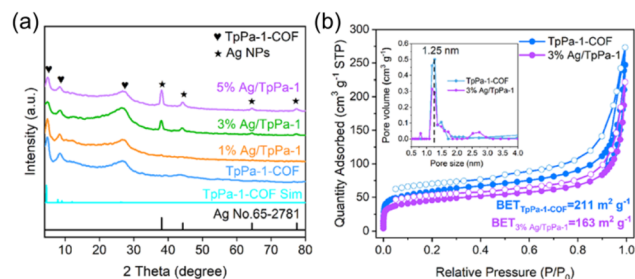

Fig. 1 (a) The PXRD patterns of a series of Ag/TpPa-1 materials. (b) N$_2$ adsorption isotherms (inset: variations in pore size).

There are obviously no additional diffraction peaks in the composites, providing evidence that the deposition of Ag metal did not influence the crystalline structure of TpPa-1-COF. Moreover, due to the low content of Ag species and their high dispersion, the 1% Ag/TpPa-1 sample does not display diffraction peaks associated with Ag. Notably, the peak diffraction intensities of Ag species increase with increasing Ag contents. These findings demonstrate that the TpPa-1-COF surface is truly deposited with Ag species.

The specific surface area and porous structure of TpPa-1-COF and 3% Ag/TpPa-1 were studied using the N$_2$ adsorption–desorption method. Fig. 1b displays the nitrogen adsorption–desorption isotherms, along with the corresponding pore size distribution curves (inset) of TpPa-1-COF and 3% Ag/TpPa-1 samples. The result demonstrates that the absorption isotherm pertains to type I, indicating the existence of microporous structures. Additionally, the hysteresis loop exhibits a type 4 shape, suggesting the existence of plate-like particles that have slit-like apertures, which are compatible with the shape of nanosheets, as displayed in Fig. S1.† The observed pore size distribution indicates a remarkable crystalline and well-organized structure, with peak maxima of around 1.25 nm. It is noteworthy that the 3% Ag/TpPa-1 sample exhibits a slightly lower BET surface area (163 m^2 g^{-1}) in contrast with the bare TpPa-1-COF sample (211 m^2 g^{-1}), apparently because the presence of Ag NPs on the surfaces of TpPa-1-COF inhibit N$_2$ molecule adsorption during the BET specific surface area measurement.
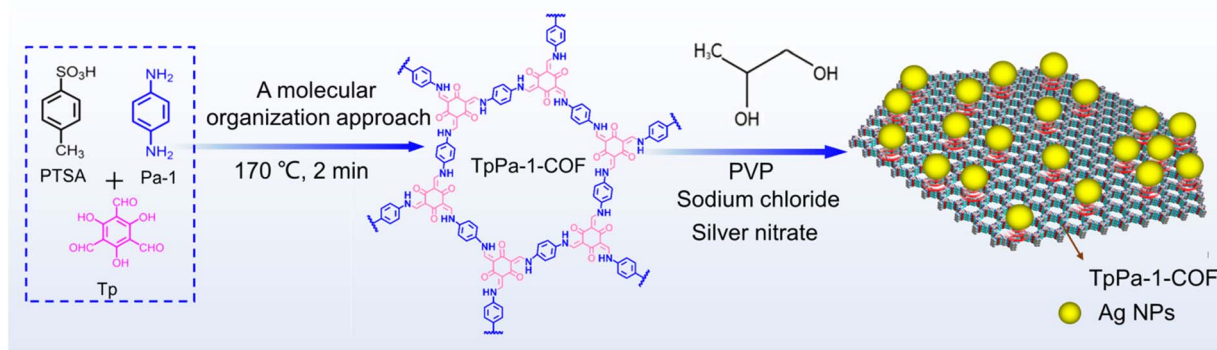
Scheme 1 Schematic depiction of the Ag/TpPa-1-COF synthesis.

The surface structural characteristics and internal microstructure of the samples were investigated using SEM, TEM, and HRTEM. Fig. 2a presents the SEM image of TpPa-1-COF. It is distinct that TpPa-1-COF exhibits relatively large and aggregated morphologies with layer structures. When compared to the pure TpPa-1-COF sample, the morphology of the sample containing 3% Ag/TpPa-1 is similar except for numerous Ag NPs with size distribution mainly at about 15 nm (Fig. 2b and c). In addition, SEM images of the 5% Ag/TpPa-1 sample indicate that some Ag NPs are closely gathered together, as observed in Fig. S1c and d.† The microstructure was further evaluated by TEM images, as shown in Fig. 2d–f. With the increase in the proportion of Ag NPs, there seems to be a certain correlation between Ag content and particle size distribution. It is noteworthy that Ag NPs co-exist in separate and adjacent contact states. Fig. 2g depicts the distribution of Ag NPs with a size of 10–30 nm on the TpPa-1-COF surface. The observed lattice fringes with a spacing measurement of $d = 0.235$ nm (Fig. 2h) can be ascribed to the presence of the (111) crystal plane attributed to the cubic phase of Ag. This finding supports the evidence of the successful synthesis of Ag/TpPa-1. Besides, HAADF-STEM was employed to perform element mapping of C, Ag, N, and O of Ag/TpPa-1 (Fig. 2i). The presence of significant signals for the elements O, Ag, N, and C in Ag/TpPa-1 further demonstrates that the samples are made up of Ag and TpPa-1-COF.

The FT-IR results are shown in Fig. 3a. As a result, the characteristic bands at approximately 3432, 1436, and 1246 cm^{-1} can be assigned to the stretching vibrations of N–H, C=C, and C–N bonds, respectively, which show almost no changes after loading Ag NPs. These bands make clear the existence of a framework structure connected to β-ketoenamine.[46] Additionally, the C=O band and the combined C=C band acting as a shoulder are responsible for the high stretching vibration peaks at 1580–1620 cm^{-1}.[15] All of these peaks correspond to the typical characteristic peaks of TpPa-1-COF. Additionally, the unmodified TpPa-1-COF sample and Ag/TpPa-1 composites have similar FT-IR spectra with no glaring differences, which, from another perspective, suggests that the introduction of Ag NPs to the TpPa-1-COF surface has no impact on the substance's structure. Additionally, the absence of an Ag representative peak in Ag/TpPa-1 composites might be attributed to the relatively low content of Ag within the composite material.

The entire XPS survey spectrum (Fig. 3b) of the 3% Ag/TpPa-1 sample is consistent with the findings of the EDS mapping analysis, showing C, N, Ag, and O elements. Fig. 3c shows the high-resolution XPS spectra of the C 1s orbital and the peaks observed at 288.8, 286.5, and 284.8 eV, which can be attributed to the C=O, C–N, and C–C/C=C bonds, respectively, and these are identical peaks to those of TpPa-1-COF. It is observed that the signal for C–C/C=C decreases with the enhanced signals for C–N after loading Ag NPs, which might be due to the disturbance and destruction of π–π stacking between the layers of TpPa-1-COF, resulting from the introduction of Ag NPs, leading to the decrease of π conjugated degree that contributes to the lower signal for C–C/C=C. Moreover, the unpaired electrons on N atoms of TpPa-1-COF might be partially coordinated with foreign exposed metal atoms (e.g., Ag) to regulate the electron density on N atoms, resulting in enhanced signals for C–N after loading Ag NPs. Peaks corresponding to the C=O bond and terminal aldehyde group are observed in both the bare TpPa-1-COF sample and the 3% Ag/TpPa-1 composites, which are depicted in Fig. 3d. Additionally, signals at these energies can be attributed to hydroxyl and adsorbed water. C–NH$_x$ groups are accountable for the strong peak at 400.4 eV in the N 1s spectra of 3% Ag/TpPa-1 (Fig. 3e). In addition, in the 3% Ag/TpPa-1 sample, the peaks of C–NH$_x$, –CHO, and C=O show a shift from the original binding energy to the higher energy by 0.34, 0.33, and 0.67 eV, respectively, compared to TpPa-1-COF. These shifts of O 1s and N 1s peaks for the 3% Ag/TpPa-1 sample can be attributed to the strong electronic interactions between Ag NPs and more electronegative O element as well as the N atoms with the unpaired electrons, and similar phenomenon was found in Pt$_1$@TpPa-1 and Ag–Pt/C$_3$N$_x$ systems.[21,47] Based on the analysis presented in Fig. 3f, Ag 3d$_{5/2}$ and 3d$_{3/2}$ are solely ascribed to the peaks at 368.6 and 374.5 eV, respectively.[39,48] There are metallic Ag^0 species present, as evidenced by the distinctive Ag 3d peak with a splitting binding energy of 5.9 eV.[45] These findings serve as supplementary evidence of the successful deposition of metallic Ag^0 onto TpPa-1-COF.

To further reveal the detailed microstructural information of Ag/TpPa-1, Ag K-edge EXAFS was performed. As illustrated in Fig. 4a, the absorption threshold (ca. 25527 eV) from the normalized Ag K-edge XANES spectra for Ag/TpPa-1 nearly matched that of the Ag foil (ca. 25527 eV) and is significantly lower than that of Ag$_2$O (ca. 25530 eV). It has been proven that Ag atoms in Ag/TpPa-1 are mostly in their valence states in Ag^0 rather than Ag$^+$. In addition, the ICP-OES measurement reveals that the real loading content of Ag NPs in the 3% Ag/TpPa-1
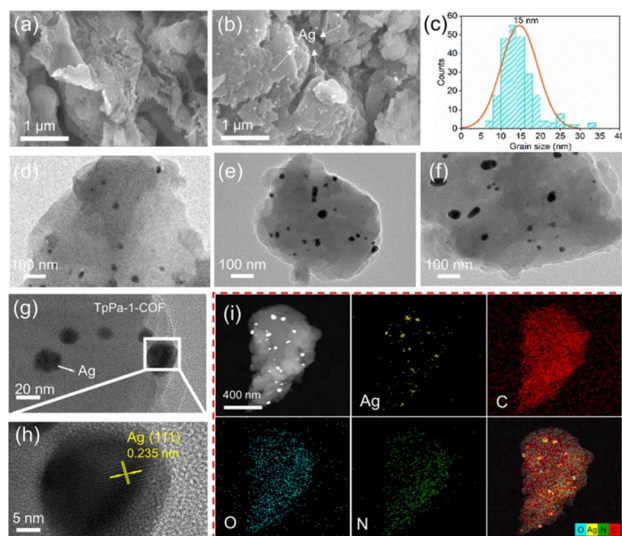

Fig. 2 SEM images of (a) TpPa-1-COF and (b) 3% AgTpPa-1. (c) Size profile of Ag NPs. (d–f) TEM images of 1% Ag/TpPa-1, 3% Ag/TpPa-1, and 5% Ag/TpPa-1. (g and h) TEM and HRTEM images of 3% Ag/TpPa-1. (i) HAADF-STEM and the corresponding elemental mappings of Ag, C, O, and N for 3% Ag/TpPa-1.
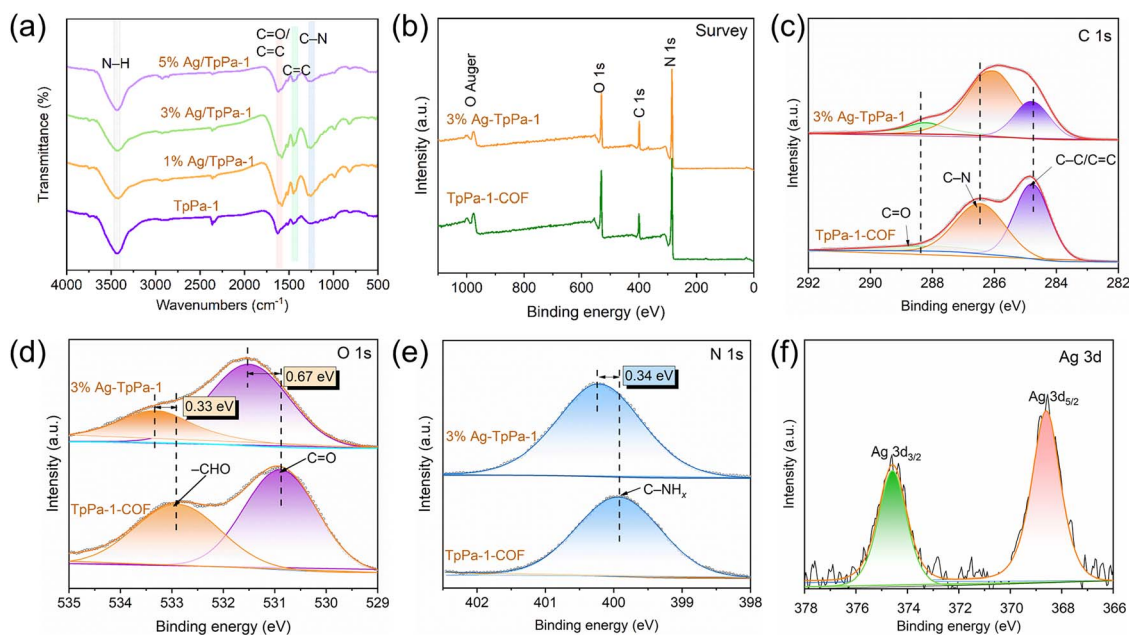
5396 | J. Mater. Chem. A, 2024, **12**, 5392–5405

This journal is © The Royal Society of Chemistry 2024

Fig. 3 (a) FT-IR spectra of the photocatalysts. XPS spectra of TpPa-1-COF and 3% Ag/TpPa-1: (b) survey XPS spectrum, (c) high-resolution XPS spectra of C 1s, (d) O 1s, (e) N 1s, and (f) Ag 3d.

sample is determined to be 0.77 wt%. Moreover, as can be seen in the Ag K-edge FT k^3-weighted EXAFS spectra (Fig. 4b), there is a dominant peak in Ag/TpPa-1 at around ~2.66 Å, which could be attributed to the Ag–Ag bonds according to the Ag foil (~2.66 Å), indicating the formation of Ag NPs. Besides, a broad band at ~1.64 Å in Ag/TpPa-1 is presented, which could be assigned to the Ag–O bonds that might be due to the coordination bond between the Ag atom and the O atom in TpPa-1-COF. As can be observed in Fig. 4d, least-squares fitting analysis for EXAFS spectra was utilized to get the quantitative structural information of Ag NPs to show the coordination numbers of Ag NPs in Ag/TpPa-1. Table S1† displays the appropriate fitting values and indicates that the coordination number of Ag is around 8 (Ag–O: 4; Ag–Ag: 4), indicating the Ag NPs load on TpPa-1-COFs by coordinating with Ag–Ag and four Ag–O. The Ag–O coordination and the small size impact of Ag nanoparticles are responsible
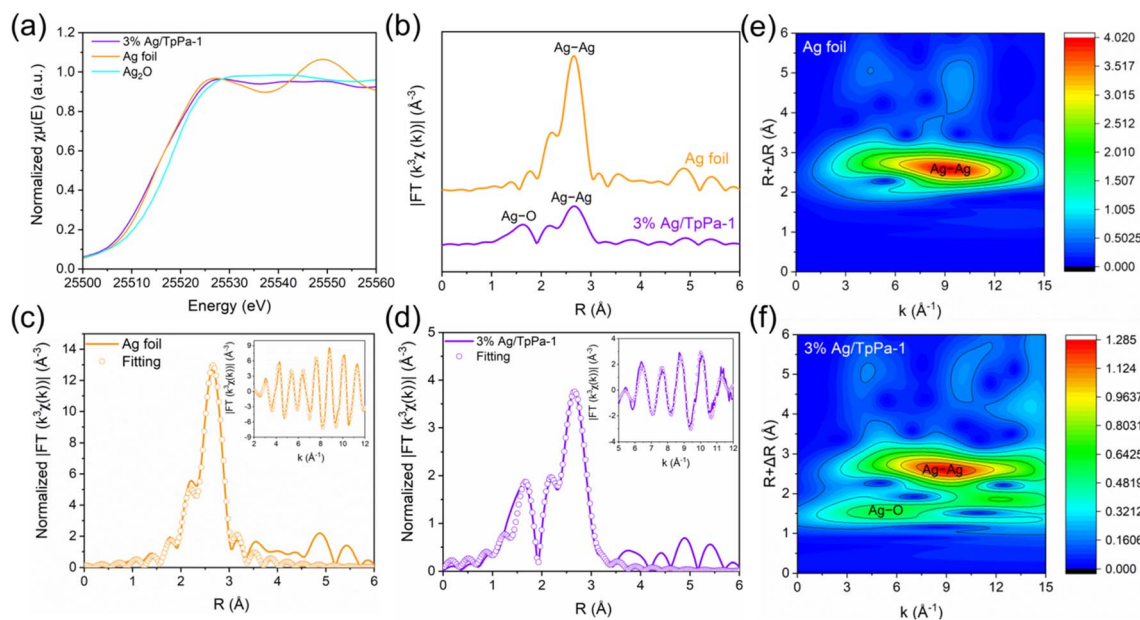

Fig. 4 (a) XANES spectra of Ag K-edge of 3% Ag/TpPa-1 sample, Ag foil, and Ag$_2$O. (b) Ag K-edge k^3-weighted FT-EXAFS spectra of 3% Ag/TpPa-1 sample and Ag foil. FT-EXAFS spectra with matching fitting curves in R and k space (inset) of (c) Ag foil and (d) 3% Ag/TpPa-1 sample. (e and f) WT-EXAFS signals of Ag foil and 3% Ag/TpPa-1 sample.

This journal is © The Royal Society of Chemistry 2024

J. Mater. Chem. A, 2024, **12**, 5392–5405 | **5397**

for the decrease in the metallic Ag–Ag coordination number for Ag/TpPa-1 when compared to Ag foil (12).[49] Furthermore, XPS results indicate a binding energy value for Ag 3d, which is attributed to the metallic Ag^0 species, and no binding energy values for Ag$_2$O, so it could be speculated that the Ag–O coordination bond is formed between Ag atom in NPs and O atom in TpPa-1. WT-EXAFS provides a way to concurrently give the radial distance resolution (R space) and the k space resolution due to its adequate resolution, as shown in Fig. 4e. It indicates that the metallic Ag–Ag bond is prominent accompanied by the partial Ag–O coordination bond in Ag/TpPa-1, further demonstrating the existence of metallic Ag NPs and the electronic interactions between Ag NPs and the TpPa-1-COF substrate.

3.2 Photocatalytic hydrogen production

The assessment of hydrogen generation through photocatalysis over each sample was conducted within a simulated visible-light environment ($\lambda \geq 420$ nm) with the sacrificial agent AC. Notably, the H$_2$ production standard curve (Fig. S2†) and the integral area of H$_2$ generated across the samples (Fig. S3 and S4†) were used to calculate the rate of H$_2$ evolution. The photocatalytic hydrogen evolution of TpPa-1-COFs loaded with different amounts of Ag NPs is presented in Fig. 5a and b. The unmodified TpPa-1-COF sample exhibits a photocatalytic hydrogen production rate of 201.9 µmol g^{-1} h^{-1}. It can be observed that hydrogen production rises when illumination time is increased. After incorporating 1% Ag NPs onto the bare TpPa-1-COF, the photocatalytic activity is significantly enhanced, resulting in an increased H$_2$ generation rate of 340.8 µmol g^{-1} h^{-1}. The photocatalytic activities of the photocatalysts are further improved by increasing the loading quantity of Ag NPs. It is noted that the hydrogen production rate for the 3% Ag/TpPa-1 composite reaches 801.2 µmol g^{-1} h^{-1}. In consequence, the deposition weight of Ag NPs has a considerable influence on photochemical activities. Specifically, the 3% Ag/TpPa-1

composite sample demonstrates a hydrogen production rate 4 times higher than that of TpPa-1-COF. The excellent performance in photocatalytic hydrogen production exhibited by the optimized 3% Ag/TpPa-1 catalyst stands out significantly when contrasted with the prior research on COF-based photocatalysts, as illustrated in Table S2.† However, when the Ag content is further increased, there is a decline in photocatalytic H$_2$ evolution once the loading content of Ag NPs is higher than 3%. Considering this, it is reasonable to conclude that an optimal deposition content of Ag NPs enables their effective distribution on the surface of TpPa-1-COF, which makes it easier to separate and transfer the charge carriers. However, an excessive quantity of Ag NPs might result in serious buildup, which could lead to a decrease in the number of available active sites and cause electrons and holes to recombine.

Recycling tests were conducted under the same settings to evaluate the stability of the 3% Ag/TpPa-1 composite. As illustrated in Fig. 5c, the rates of H$_2$ evolution during photocatalysis by 3% Ag/TpPa-1 composite exhibit only a marginal decrease over five consecutive cycles, with a total reaction time of 30 hours. The corresponding XRD pattern and FTIR spectrum of 3% Ag/TpPa-1 after photocatalysis match well with that of the fresh 3% Ag/TpPa-1 (Fig. S5a and b†), indicating that its crystallinity and microstructures are well retained. The XPS spectrum and TEM image (Fig. S5c and d†) indicate that the Ag NPs in Ag/TpPa-1 remained in the Ag^0 state and did not fall off after the photocatalytic reaction. This observation highlights the remarkable stability and sustained photocatalytic properties of the Ag/TpPa-1 photocatalyst. The DRS curves and the wavelength-dependent AQE of 3% Ag/TpPa-1 are closely matched (Fig. 5d), suggesting that the reaction was sparked by incoming photon absorption. At 450 nm for 3% Ag/TpPa-1, the maximum AQE of 1.2% was recorded, which is associated with the strongest LSPR peak of Ag NPs at 465 nm, as confirmed by Fig. 6a.

3.3 Dynamics of photogenerated carriers

UV-Vis DRS was utilized to characterize and illustrate the optical absorption characteristics of the as-prepared samples. Based on the data presented in Fig. 6a, it can be observed that Ag/TpPa-1 composites exhibit uniform light absorption across the UV-Vis DRS spectrum. Moreover, the absorption edge of Ag/TpPa-1 composites is obviously red-shifted (*ca.* 50 nm) compared with bare TpPa-1-COF, indicating that the deposition of Ag NPs can expend the visible-light response range of TpPa-1, which might be due to the increased refractive index after loading Ag NPs and/or the strong electronic interaction between the support and Ag NPs.[50,51] Because the radius of Ag atoms is too large (1.75 Å), it is not easy to be doped into the crystal lattice of TpPa-1. Indeed, the Ag/TpPa-1-COF is the composite of Ag and TpPa-1-COF, which exhibits the mixed optical behavior of pristine Ag and TpPa-1-COF rather than the reduced band gap. Furthermore, a significant enhancement of the absorption peak at approximately 465 nm is observed in the Ag/TpPa-1 sample, which is identified as the LSPR effect of Ag NPs. The LSPR effect of Ag NPs is also responsible for a substantial enhancement in
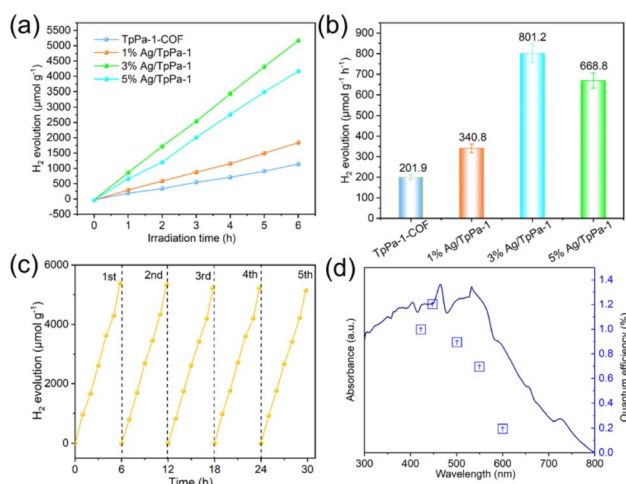

Fig. 5 (a) Performance of time-dependent photocatalytic H$_2$ evolution. (b) Photocatalytic H$_2$ evolution by all the samples. (c) Tests on the development of H$_2$ over 3% Ag/TpPa-1 during cycles. (d) The dependence of AQE on wavelength for 3% Ag/TpPa-1.

5398 | *J. Mater. Chem. A*, 2024, **12**, 5392–5405

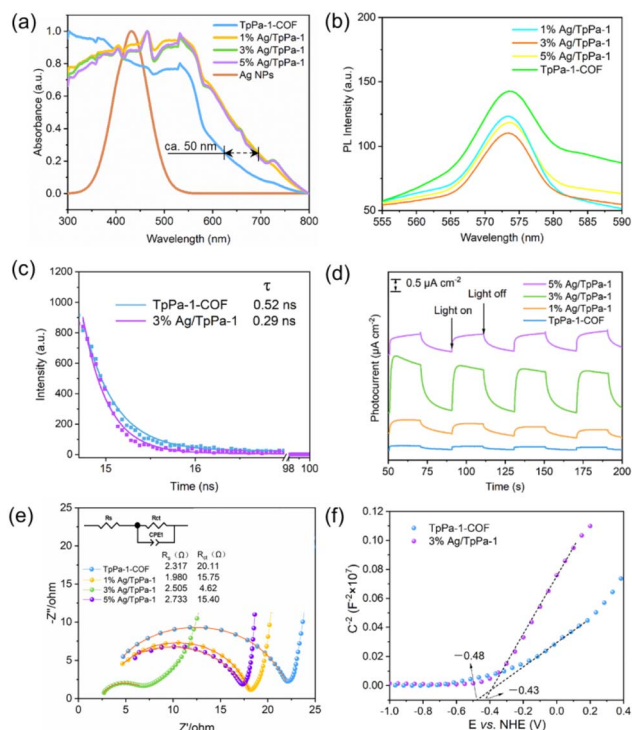This journal is © The Royal Society of Chemistry 2024

Fig. 6 (a) UV-vis DRS of the as-prepared samples. (b) Steady-state PL spectra excited by a wavelength of 380 nm. (c) Transient PL decay profiles. (d) Transient photocurrent responses. (e) EIS Nyquist plots. (f) Mott−Schottky plots.

light harvesting in the visible spectrum. Thus, the increased visible light capture capacity of Ag/TpPa-1 composites facilitates the generation of additional photon-generated carriers; thereby, the system's photocatalytic properties are enhanced.

The transfer and recombination kinetics of photogenerated carriers are frequently studied using the PL spectra. In general, a photocatalyst exhibiting high PL intensity indicates a higher likelihood of electron–hole pair recombination, whereas a photocatalyst with low PL intensity suggests a higher efficiency in charge separation. Fig. 6b displays the PL spectra of a series of samples. The PL peaks of the Ag/TpPa-1 composites are notably smaller compared to those of TpPa-1-COF. This observation provides evidence that the incorporation of Ag NPs effectively enhances charge transfer efficiency and hinders the recombination of photogenerated electrons and holes. Among various Ag/TpPa-1 composites, the 3% Ag/TpPa-1 photocatalyst demonstrates the smallest intensity of the PL spectrum absorption peak. This finding suggests the highest efficiency in charge carrier separation and the lowest rate of charge recombination, aligning with the results obtained from the photocatalytic hydrogen rate. To better comprehend the charge dynamics, we measured the PL decay curves of both TpPa-1-COF and 3% Ag/TpPa-1 (Fig. 6c). The decay profiles of the time-resolved PL were analyzed by fitting them with single-exponential functions. The analysis reveals that the incorporation of Ag NPs results in a reduced lifetime, such as 0.29 ns for the 3% Ag/TpPa-1 composite, in contrast to TpPa-1 alone, which

has a lifetime of 0.52 ns. This result suggests that the distance of carrier migration between the Ag NPs and TpPa-1-COF is shortened through an additional decay pathway.

The substantial light-harvesting ability (Fig. 6a) caused by the local electric field is subsequently translated into a higher rate of electron–hole pair generation on the surface of the photocatalyst as opposed to in bulk, giving the photogenerated carriers a shorter diffusion length, a lower probability of recombination, and more opportunities to take part in the surface photocatalytic reaction.[52,53] Besides that, as seen by the decreased PL peak intensity (Fig. 6b), the LSPR-induced local electric field also promotes spatial charge separation and directs charge migration toward active sites to further activate the photocatalytic process.[54,55] This is because the metal Ag NPs' surface has an enhanced local electric field that extends tens of nanometers outward from the surface.[40] This could lead to the potential separation of more photogenerated electron–hole pairs and the presentation of a close-range dipole–dipole resonance at the interface between semiconductors (like TpPa-1-COF) and metals (like Ag NPs). Notably, the excited electrons in the semiconductor (such as TpPa-1-COF) are mostly situated in the shallow position under the surface, enabling a very short diffusion distance to the surface.[40] As a result, electron–hole pairs might be quickly created close to the semiconductor surface and rapidly travel to the surface to participate in the photocatalytic H_2 evolution event because of the increased local electric field.

Analyzing transient photocurrent responses and electrochemical impedance spectroscopy (EIS) plots allowed researchers to better understand how photogenerated electrons and holes are separated at the composite photocatalyst's interface. Over a few on-off photoirradiation cycles, the transient photocurrent responses of Ag/TpPa-1 reveal an increasing photoinduced charge separation (Fig. 6d). Especially the 3% Ag/TpPa-1 composite has the strongest photocurrent response than other photocatalysts, indicating that it has the most effective means of separating and transferring photoinduced carriers. The performance of photocatalytic hydrogen generation is also consistent with this photocurrent intensity. Subsequently, electrochemical impedance tests were conducted to study charge separation and transport mechanisms. Fig. 6e illustrates the Nyquist impedance plots obtained from the EIS measurements conducted on the prepared samples. The radius of 3% Ag/TpPa-1 is remarkably smaller compared with that of TpPa-1-COF. Additionally, the charge-transfer resistance (R_{ct}) steadily decreases from 20.11 kΩ in TpPa-1-COF to 4.62 kΩ in 3% Ag/TpPa-1. Overall, the photogenerated charge separation is improved in the 3% Ag/TpPa-1 composite compared to TpPa-1-COF, which is completely in conformity with the findings of photocatalytic hydrogen production efficiency. Fig. 6f presents the results of the Mott–Schottky analysis, which was conducted to determine the energy level of the conduction band minimum (E_{CBM}), which is −0.43 V vs. normal hydrogen electrode (NHE) for TpPa-1 and −0.48 V vs. NHE for the 3% Ag/TpPa-1 composite, indicating that the E_{CBM} value of TpPa-1-COF is slightly changed after loading Ag NPs.

This journal is © The Royal Society of Chemistry 2024

J. Mater. Chem. A, 2024, **12**, 5392–5405 | **5399**

3.4 FDTD simulation

The LSPR effects could increase the interfacial electric field, generate hot electrons, and give additional absorption peaks in the visible light range.[56] Moreover, the increased local interfacial electric field could significantly facilitate hot electrons' ability to cross the surface.[56] Furthermore, when a plasmonic metal's LSPR mode is excited, the energy of the conduction band electrons rises above the metal's Fermi level, producing what are known as "hot electrons," which are then susceptible to a nonradiative decay *via* Landau damping.[52] Besides, large electric field enhancements could result in "hot spots" in the interparticle gap area,[57,58] particularly in the gap area between two strongly coupled Ag or Au NPs.[59] In addition, FDTD simulation of adjacent nanoparticle pairs is usually employed to reflect the "hot spots" region in the junction.[58,60] Especially, the "hot spots" effects through the FDTD simulation were used to describe the enhanced localized electric field in the field of photocatalysis.[31,61] Therefore, the FDTD simulation as an indicator of localized electric field enhancement was used to describe the "hot spots" effects in this work.

Theoretically, the LSPR linking up a photocatalyst and a plasma metal could intensify the local electric field enhancement factor (EF) and "hot spots".[31,61,62] The interfacial electric field EF distribution resulting from the LSPR effect-induced hot electron injection at the Ag/TpPa-1-COF interface was simulated using three-dimensional FDTD in order to better comprehend the aforementioned impact. To investigate the wavelength-dependent LSPR effect, a simplified model was established (Fig. 7a). As shown in Fig. 7b–d, the interfacial electric field EF distribution is clearly shown under the irradiation of light at three different excitation wavelengths (420, 465, and 500 nm). These selected wavelengths of light are closely related to the region of the LSPR effect in the UV-Vis DRS. The FDTD simulation results indicate the presence of LSPR-enhanced "hot spots" near the edge of plasmonic Ag NPs in

the Ag/TpPa-1 interface, which facilitates high-energy charge carrier generation by using the energy of incident light with various wavelengths. Based on the simulated interfacial electric field EF distribution, the maximum EF (*i.e.*, $|E|/|E_0|$) is obtained at the incident wavelength of 465 nm, where E is the local electric field and E_0 is the incident source electric field. This agrees with what we have seen with the LSPR effect from the UV-Vis DRS spectra.

Moreover, the effect of the numbers of Ag NPs (*e.g.*, 2, 3, 4, 5, 6, and 7) on the simulated interfacial electric field $|E|/|E_0|$ distribution excited at $\lambda = 465$ nm was investigated using the FDTD method, as shown in Fig. 8. When Ag NPs are isolated and dispersed on the surface of TpPa-1-COFs (Fig. 8a–d), the "hot spots" region becomes enlarged as the number of Ag NPs increases. When the number of Ag NPs exceeds 5, the "hot spots" region becomes overlapping (Fig. 8e and f), which is attributed to the coupling effect of the "hot spots". Moreover, the accurate values of the electric field EF of Ag NPs, TpPa-1-COF, and total model of Ag/TpPa-1 could be obtained from the surface integral, and the results are shown in Fig. 8h. It is found that the total $|E|/|E_0|$ of Ag/TpPa-1 with various numbers of Ag NPs of 1, 2, 3, 4, 5, 6, and 7 is 1.038×10^4, 1.0404×10^4, 1.0416×10^4, 1.0429×10^4, 1.0442×10^4, 1.0451×10^4, and 1.0442×10^4, respectively. Clearly, when six adjacent Ag NPs gather together, the total electric field EF reaches the maximum, and then a slight decrease of the total electric field EF is found when seven Ag NPs closely aggregate together. This is due to the coupling effect of the "hot spots" (*i.e.*, the junction of neighboring Ag NPs), as presented in Fig. 8e and f, which enables Ag NPs to enhance the hot electron production rate more efficiently, as it is proportional to the electric field strength. However, it is observed that the area of the "hot spots" becomes smaller when seven Ag NPs closely aggregated together (Fig. 8g) compared with the case where six Ag NPs gathered together (Fig. 8f), which might result from the electric field shielding effect when much more Ag NPs closely aggregated together, leading to the decrease in the generation of the hot electron. This could be used to account for the decrease in the photocatalytic H_2 evolution rate of 5% Ag/TpPa-1, in which some Ag NPs closely aggregated together (as confirmed by Fig. S1c and d†), which might induce the decrease in the electric field intensity and the reduction of the area of the "hot spots". Therefore, the simulated interfacial electric field $|E|/|E_0|$ distribution of Ag/TpPa-1 with different numbers of Ag NPs demonstrates that the optimal value of Ag NPs leads to the largest electric field EF accompanied by the maximal "hot spots" region, which means much more hot electrons could be produced, resulting in the sample with 3% Ag/TpPa-1 having the best photocatalytic H_2 evolution capability.

Furthermore, the interfacial electric field EF of Ag/TpPa-1 with different sizes of Ag NPs was simulated by gradually introducing one Ag NP with sizes of 18, 16, 14, 12, 10, and 8 nm, respectively, as illustrated in Fig. 9a–g, since TEM results indicate that the distribution of Ag NPs is non-uniform and the main particle size distribution of Ag NPs is around 15 nm. The simulation results show that the LSPR effect may lead to a localized enhancement of the electric field intensity within
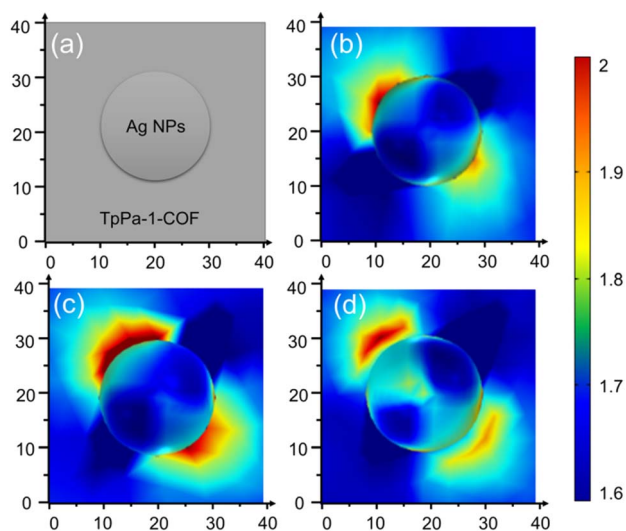

Fig. 7 (a) Simulated model of Ag/TpPa-1. Simulated interfacial electric field $|E|/|E_0|$ distribution of Ag/TpPa-1 at excitation wavelengths of 420 nm (b), 465 nm (c), and 500 nm (d).

5400 | *J. Mater. Chem. A*, 2024, **12**, 5392–5405

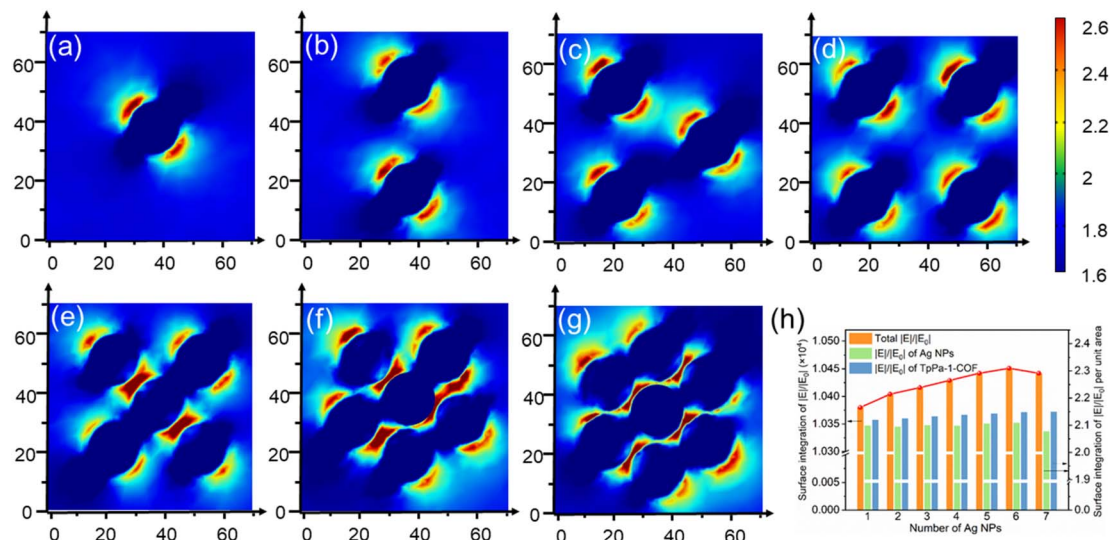This journal is © The Royal Society of Chemistry 2024

Fig. 8   Simulated interfacial electric field $|E|/|E_0|$ distribution of Ag/TpPa-1 with different numbers of Ag NPs excited at $\lambda = 465$ nm: (a) single Ag NPs, (b) two Ag NPs, (c) three Ag NPs, (d) four Ag NPs, (e) five Ag NPs, (f) six Ag NPs, and (g) seven Ag NPs. (h) Surface integration of $|E|/|E_0|$.
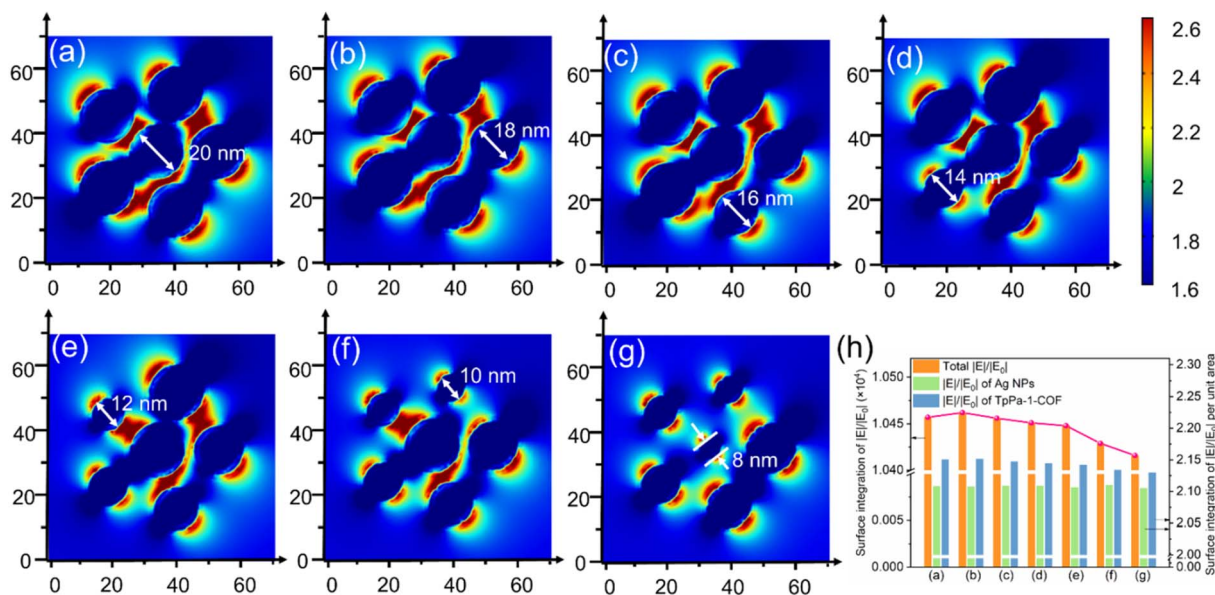

Fig. 9   Simulated interfacial electric field $|E|/|E_0|$ distribution of Ag/TpPa-1 through a gradual introduction of a smaller diameter of Ag NPs excited at $\lambda = 465$ nm: (a) 20 nm, (b) 18 nm, (c) 16 nm, (d) 14 nm, (e) 12 nm, (f) 10 nm, and (g) 8 nm. (h) Surface integration of $|E|/|E_0|$.

a certain range as the particle size of Ag NPs decreases. However, as the particle size of Ag NPs continues to decrease, the electric field EF begins to decrease. This is because the coupling effect of the "hot spots" is significantly decreased, resulting from the distance between two Ag NPs with different sizes being enlarged when many more Ag NPs with smaller sizes are introduced. The variation of the electric field EF of Ag NPs, TpPa-1-COF, and total model of Ag/TpPa-1 is illustrated in Fig. 9h. By observing the surface integral of total $|E|/|E_0|$, it can be found that the maximum electric field EF is presented when the particle size of Ag NPs reaches 18 nm. These results indicate

that the diameter of the Ag NPs plays an important role in the electric field EF of Ag/TpPa-1.

Additionally, the LSPR-enhanced localized electric field distribution depends on the alignment and relative position of plasmonic metal NPs.[31] Therefore, the effect of the gap distance of Ag NPs on the electric field EF was further investigated, as illustrated in Fig. 10. It is found that the area of the "hot spots" region enlarges gradually, accompanied by an increasing gap distance between two neighboring Ag NPs. However, when the gap distance is greater than 10 nm, the interaction between two neighboring Ag NPs could be weakened, which reduces the total
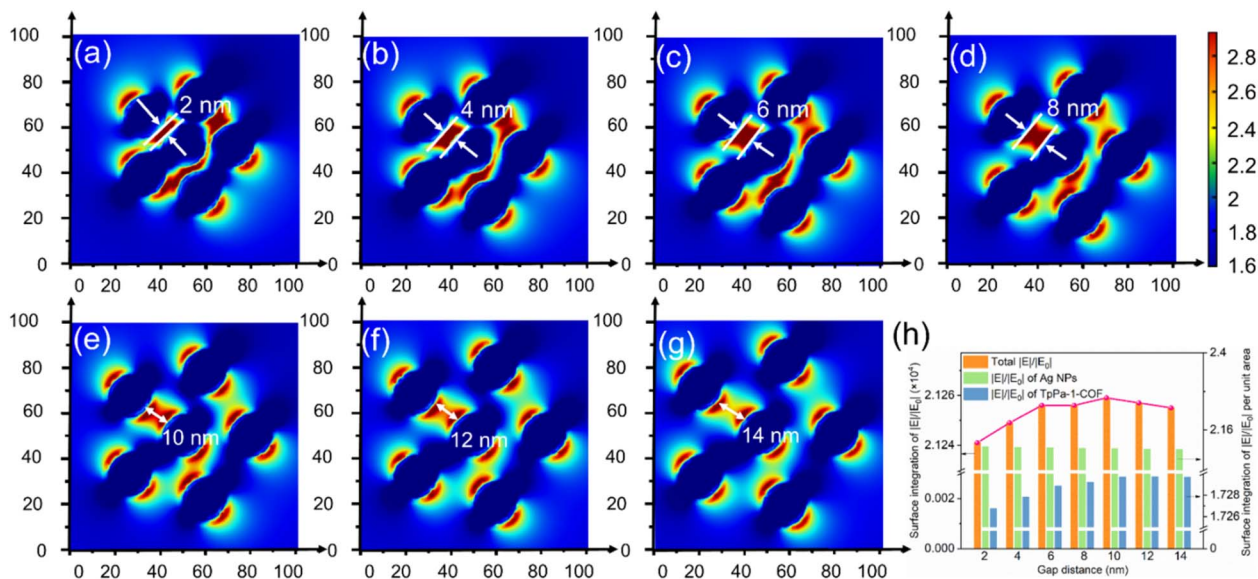
Fig. 10 Simulated interfacial electric field $|E|/|E_0|$ with different gap distances of Ag NPs excited at $\lambda = 465$ nm: (a) 2 nm, (b) 4 nm, (c) 6 nm, (d) 8 nm, (e) 10 nm, (f) 12 nm, and (g) 14 nm. (h) Surface integration of $|E|/|E_0|$.

electric field EF, resulting from a weakening of the coupling effect of "hot spots".

3.5 DFT calculations

To further comprehend the catalytic active site of Ag/TpPa-1, DFT calculations were used. Because the radius of Ag atoms is too large, it is not easy to be doped into the crystal lattice of TpPa-1. Thus, a geometric model with a single TpPa-1-COF (001) planar unit cell and an Ag13 cluster was employed to complete the DFT calculations, as shown in Fig. S6.† The density of state (DOS) indicates that the CB of Ag/TpPa-1 is closer to the Fermi level than that of TpPa-1 (Fig. 11a and b), demonstrating that
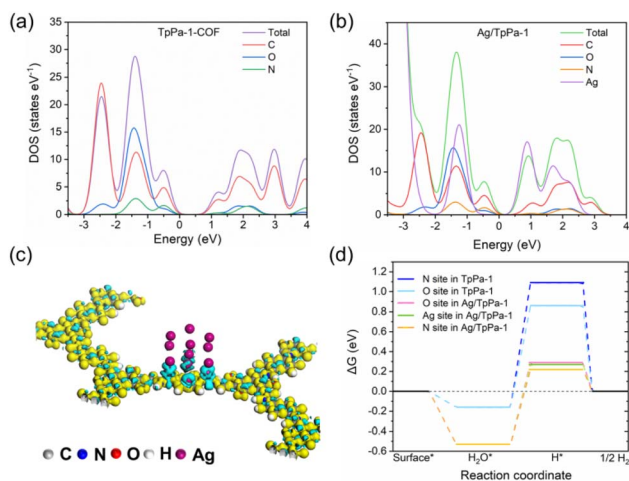

Fig. 11 (a) DOS of TpPa-1-COF sand (b) Ag/TpPa-1. (c) Charge density difference maps (the blue zone denotes charge depletion, whereas the yellow region symbolizes charge buildup). (d) H_2 evolution reaction free energy profiles over TpPa-1-COFs and Ag/TpPa-1 with different adsorbed sites.

Ag/TpPa-1 has greater charge transfer efficiency and a larger carrier density.[63] The differential charge density diagram shows that Ag NPs are mostly controlled by the blue area while TpPa-1 is principally filled by the yellow area (Fig. 11c), demonstrating a quicker electron transport across the interface from Ag NPs to TpPa-1. As illustrated in Fig. S7,† a three-state schematic representing the initial catalyst-H_2O^* adsorption state, the intermediate catalyst-H^* state, and the end catalyst-H_2 product state was used to depict the whole HER process.[64] As shown in Fig. 11d, the Gibbs free energy of H_2O molecule adsorption ($\Delta G_{H_2O^*}$) on the Ag/TpPa-1 (-0.53 eV) is more negative than that on the TpPa-1 site (-0.16 eV), indicating that Ag/TpPa-1 is more favorable for H_2O molecule adsorption. Moreover, the Gibbs free energy associated with the atomic hydrogen adsorption, ΔG_{H^*}, has been accepted as a reliable marker for assessing the HER's catalytic activity. In general, ΔG_{H^*} can vary depending on the adsorption sites of the H atom and the configurations.[65] It is possible to identify the most active adsorption site as the one with the lowest $|\Delta G_{H^*}|$.[66,67] Therefore, the ΔG_{H^*} values for every potential adsorption site in many models were calculated (Fig. S8†). It is found that both the N and O sites in TpPa-1-COFs for adsorbing one H atom exhibit comparatively large ΔG_{H^*} values of 1.09 and 0.86 eV, respectively. The large ΔG_{H^*} values for both the N and O sites in TpPa-1-COFs could be ascribed to the following two reasons. Firstly, the H atom is preferentially adsorbed on the N and O sites in TpPa-1-COFs within a 2D plane (Fig. S8a and b†), resulting in the H atom firmly bonding to the N and O sites through in-plane sp^2 orbitals.[68] Secondly, the adsorbed H atom could interact with other H atoms of TpPa-1-COFs within the in-plane through substantial charge density overlapping (Fig. S8a and b†), which could strengthen this H atom's binding.[68,69] Moreover, it is discovered that the ΔG_{H^*} of a hydrogen atom adsorbed on the N sites in Ag/TpPa-1 (0.22 eV) is closer to 0, compared with that adsorbed on the Ag sites in Ag/

5402 | *J. Mater. Chem. A*, 2024, **12**, 5392–5405

This journal is © The Royal Society of Chemistry 2024

TpPa-1 (0.27 eV) and the O sites in Ag/TpPa-1 (0.29 eV). It indicates that the H–N binding in Ag/TpPa-1 is significantly weaker than in TpPa-1. This is because the introduction of Ag atoms pushes the H bound onto N out of the TpPa-1 in-plane, resulting in a substantial decrease in the charge density interaction between H and N as well as the H–N bonding (Fig. S8e†). Furthermore, this result suggests that there is a preferential desorption of molecular hydrogen on the N sites in Ag/TpPa-1 and favorable electron–proton transfer to form H*. Additionally, the preferential N sites in Ag/TpPa-1 could ensure both effective production of H* through the interaction of H$^+$ and e$^-$ and subsequently quick hydrogen desorption. In contrast, pure TpPa-1 has a noticeably greater ΔG_{H*}, indicating that the hydrogen adsorption is too powerful to be desorbed.

3.6 Mechanism analysis

According to the aforementioned findings, we present a preliminary photocatalytic process to elucidate the remarkable charge transfer and photocatalytic activity in Ag/TpPa-1 composite photocatalysts. It is generally considered that there are two different mechanisms for the composite of semiconductor and noble metal, such as the Schottky junction and plasmonic effect, which depend on their work functions and the type of semiconductor.[70] Several aspects can impact the band diagram at the interface between a semiconductor and a plasmonic metal. Band bending in the semiconductor is typically the result of these factors, which also include their work function, Fermi energy alignment, and the particular arrangement of the material surface states.[71,72] When the work function of the plasmonic metal is smaller than that of the n-type

semiconductor, a downward band bend of the n-type semiconductor would be formed due to the electron migration, which may significantly quicken reaction kinetics.[69] In this case, the TpPa-1-COF is an n-type semiconductor and its work function (4.82 eV) is larger than that of Ag metal (4.26 eV).[23,73] Thereby, when there is contact, it follows the mechanism of the plasmonic effect. It would allow hot electrons from the plasmonic Ag caused by the LSPR effect to flow to the LUMO of TpPa-1-COF, causing a downward band bend of TpPa-1-COF until the equilibrium is reached at the Fermi level, as illustrated in Scheme 2a. A similar mechanism was reported between Ag and BiOCl (001) in the composite of Ag/BiOCl, in which the band of BiOCl bends downward, and the plasma hot carrier injection was realized to enhance photocatalytic performance.[74] It is also noted that the electron migration direction is supported by the results from the differential charge density diagram based on DFT calculations as mentioned above (Fig. 11c). It means that Ag NPs act as a plasmonic metal to generate hot electrons rather than cocatalysts in the Ag/TpPa-1 composite in this case. Moreover, the ability to collect visible light is improved in the Ag/TpPa-1 composites due to the LSPR action of Ag NPs deposited onto the TpPa-1-COF surface. Additionally, the LSPR phenomenon of Ag NPs with optimal numbers, particle size, and gap distance causes an amplification of the localized electric field and the maximal "hot spots" region, resulting in much more hot electrons being produced, as confirmed by Fig. 7–10 as mentioned above. As depicted in Scheme 2b, when subjected to visible light irradiation, the Ag/TpPa-1 photocatalytic systems exhibit the generation of plasmonic states of Ag NPs. This is because the plasma action of Ag NPs causes a resonance between the incident light and off-
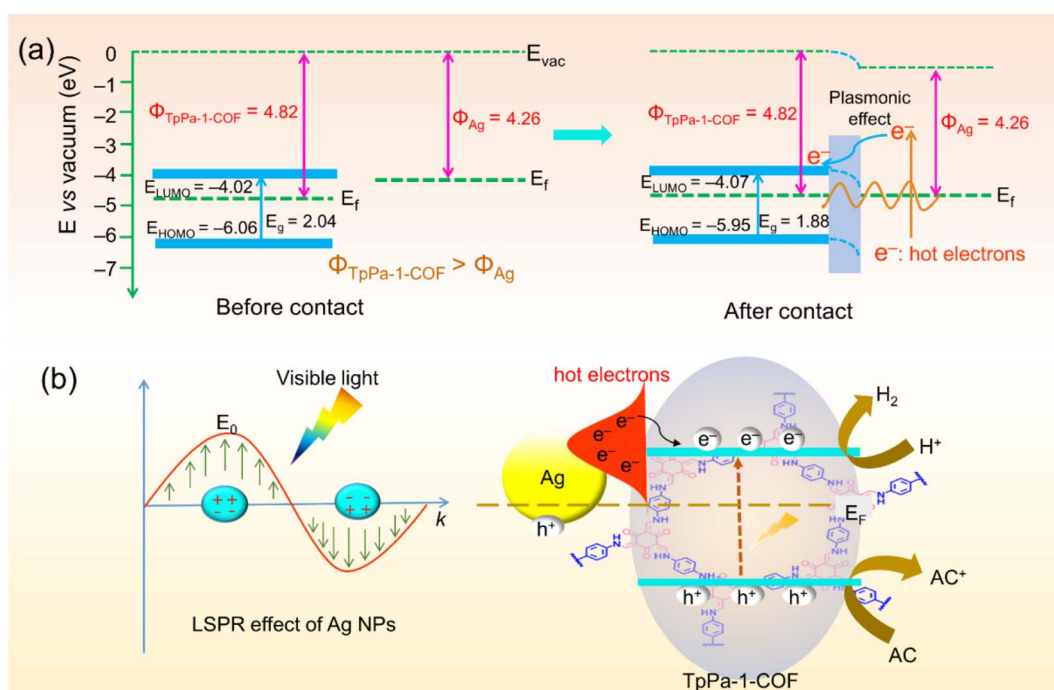
Scheme 2 (a) Diagrams depicting the energy band location and the Fermi level of TpPa-1-COF and Ag NPs before and after contact. (b) A suggested mechanism for the release of H$_2$ by photocatalysis over Ag/TpPa-1.

domain electrons. Energy transfer from the plasma of Ag NPs to TpPa-1-COF occurs through hot electrons. The energetic hot electrons produced by Ag NPs can immediately immigrate to the CB of TpPa-1-COF, which are engaged in the reduction process of H^+ to H_2, and the holes at the VB of TpPa-1-COF could react with AC as a sacrificial regent in the meanwhile. During this process, the lower ΔG_{H*} of the preferential N sites in Ag/TpPa-1 (Fig. 11d) significantly improves the interaction of H^+ and e^- and subsequently quick hydrogen desorption, resulting in enhanced photocatalytic H_2 production performance.

4. Conclusion

In conclusion, we developed an *in situ* approach to preparing the Ag/TpPa-1 photocatalytic water-splitting catalyst. By making the absorption of visible light as efficient as possible due to the LSPR effect in the Ag/TpPa-1 sample, hydrogen generation efficiency could be raised even more, reaching 801.2 μmol g^{-1} h^{-1}. Moreover, the LSPR effect of Ag NPs contributes to the Ag/TpPa-1 photocatalyst achieving an AQE of 1.2% at 450 nm. Furthermore, the FDTD simulations show that the wavelength of an excited LSPR has a direct relationship to how strong the electric field is at the interface, and its strongest electric field intensity with an excitation wavelength of 465 nm is consistent with the UV-Vis DRS spectrum. In the case of the same incident light, the strongest total electric field EF is presented when the number of Ag NPs reaches 6. Besides, it has been demonstrated that the LSPR-enhanced localized electric field distribution highly depends on the particle size and gap distance of Ag NPs. Additionally, DFT results demonstrate the hot electron transfer from Ag NPs to TpPa-1 across the interface and the preferential N sites in Ag/TpPa-1 possess both effective production of H* and subsequently quick hydrogen desorption compared with O sites and Ag sites in Ag/TpPa-1. Overall, this research opens the door to enhancing the plasmonic hot electron injection and reducing the energy barrier for sustainable photocatalytic hydrogen generation.

Author contributions

Lihua Zhang: investigation, data curation, visualization, writing – original draft. Xu Lu: methodology. Jiaqi Sun: software. Cunxia Wang: validation. Pengyu Dong: conceptualization, funding acquisition, supervision, writing – review, and editing.

Conflicts of interest

There are no conflicts to declare.

Acknowledgements

Notes and references

1 T. Hisatomi and K. Domen, *Nat. Catal.*, 2019, **2**, 387–399.
2 X. Wang, L. Chen, S. Y. Chong, M. A. Little, Y. Wu, W.-H. Zhu, R. Clowes, Y. Yan, M. A. Zwijnenburg and R. S. Sprick, *Nat. Chem.*, 2018, **10**, 1180–1189.
3 Z. Wang, C. Li and K. Domen, *Chem. Soc. Rev.*, 2019, **48**, 2109–2125.
4 S. Cao and L. Piao, *Angew. Chem., Int. Ed.*, 2020, **59**, 18312–18320.
5 S. Ma, T. Deng, Z. Li, Z. Zhang, J. Jia, Q. Li, G. Wu, H. Xia, S. W. Yang and X. Liu, *Angew. Chem., Int. Ed.*, 2022, **134**, e202208919.
6 S. J. A. Moniz, S. A. Shevlin, D. J. Martin, Z.-X. Guo and J. Tang, *Energy Environ. Sci.*, 2015, **8**, 731–759.
7 S. Zhu and D. Wang, *Adv. Energy Mater.*, 2017, **7**, 1700841.
8 M. Melchionna and P. Fornasiero, *ACS Catal.*, 2020, **10**, 5493–5501.
9 L. H. Shao, A. X. Huang, X. C. Yan, Y. H. Liu, Y. Wang, X. Jin and F. M. Zhang, *J. Colloid Interface Sci.*, 2023, **633**, 233–242.
10 H. Zhao, Q. Mao, L. Jian, Y. Dong and Y. Zhu, *Chin. J. Catal.*, 2022, **43**, 1774–1804.
11 H. Wang, H. Wang, Z. Wang, L. Tang, G. Zeng, P. Xu, M. Chen, T. Xiong, C. Zhou, X. Li, D. Huang, Y. Zhu, Z. Wang and J. Tang, *Chem. Soc. Rev.*, 2020, **49**, 4135–4165.
12 J. L. Segura, S. Royuela and M. Mar Ramos, *Chem. Soc. Rev.*, 2019, **48**, 3903–3945.
13 C. Xia, K. O. Kirlikovali, T. H. C. Nguyen, X. C. Nguyen, Q. B. Tran, M. K. Duong, M. T. Nguyen Dinh, D. L. T. Nguyen, P. Singh, P. Raizada, V.-H. Nguyen, S. Y. Kim, L. Singh, C. C. Nguyen, M. Shokouhimehr and Q. V. Le, *Coord. Chem. Rev.*, 2021, **446**, 214117.
14 H. Liu, D. Wang, Z. Yu, Y. Chen, X. Li, R. Zhang, X. Chen, L. Wu, N. Ding, Y. Wang and Y. Zhao, *Sci. China Mater.*, 2023, **66**, 2283–2289.
15 S. Kandambeth, A. Mallick, B. Lukose, M. V. Mane, T. Heine and R. Banerjee, *J. Am. Chem. Soc.*, 2012, **134**, 19524–19527.
16 B. P. Biswal, S. Chandra, S. Kandambeth, B. Lukose, T. Heine and R. Banerjee, *J. Am. Chem. Soc.*, 2013, **135**, 5328–5331.
17 H. Shen, D. Shang, L. Li, D. Li and W. Shi, *Appl. Surf. Sci.*, 2022, **578**, 152024.
18 F. M. Zhang, J. L. Sheng, Z. D. Yang, X. J. Sun, H. L. Tang, M. Lu, H. Dong, F. C. Shen, J. Liu and Y. Q. Lan, *Angew. Chem., Int. Ed.*, 2018, **57**, 12106–12110.
19 C. C. Li, M. Y. Gao, X. J. Sun, H. L. Tang, H. Dong and F. M. Zhang, *Appl. Catal., B*, 2020, **266**, 118586.
20 J. L. Sheng, H. Dong, X. B. Meng, H. L. Tang, Y. H. Yao, D. Q. Liu, L. L. Bai, F. M. Zhang, J. Z. Wei and X. J. Sun, *ChemCatChem*, 2019, **11**, 2313–2319.
21 P. Dong, Y. Wang, A. Zhang, T. Cheng, X. Xi and J. Zhang, *ACS Catal.*, 2021, **11**, 13266–13279.
22 Y. Wang, P. Dong, K. Zhu, A. Zhang, J. Pan, Z. Chen, Z. Li, R. Guan, X. Xi and J. Zhang, *Chem. Eng. J.*, 2022, **446**, 136883.
23 P. Dong, T. Cheng, J.-l. Zhang, J. Jiang, L. Zhang, X. Xi and J. Zhang, *ACS Appl. Energy Mater.*, 2023, **6**, 1103–1115.

24 P. Dong, A. Zhang, T. Cheng, J. Pan, J. Song, L. Zhang, R. Guan, X. Xi and J. Zhang, *Chin. J. Catal.*, 2022, **43**, 2592–2605.

25 S. Linic, P. Christopher and D. B. Ingram, *Nat. Mater.*, 2011, **10**, 911–921.

26 C. Clavero, *Nat. Photonics*, 2014, **8**, 95–103.

27 Y. Shang, H. Fan, X. Yang, W. Dong and W. Wang, *J. Colloid Interface Sci.*, 2023, **631**, 269–280.

28 H. Y. Liu, C. G. Niu, H. Guo, D. W. Huang, C. Liang, Y. Y. Yang, N. Tang and X. G. Zhang, *J. Colloid Interface Sci.*, 2022, **610**, 953–969.

29 N. Wu, *Nanoscale*, 2018, **10**, 2679–2696.

30 M. Rycenga, C. M. Cobley, J. Zeng, W. Li, C. H. Moran, Q. Zhang, D. Qin and Y. Xia, *Chem. Rev.*, 2011, **111**, 3669–3712.

31 X. Jiang, J. Huang, Z. Bi, W. Ni, G. Gurzadyan, Y. Zhu and Z. Zhang, *Adv. Mater.*, 2022, **34**, 2109330.

32 J. M. McMahon, S. Li, L. K. Ausman and G. C. Schatz, *J. Phys. Chem. C*, 2012, **116**, 1627–1637.

33 Y. Liu, S. Pedireddy, Y. H. Lee, R. S. Hegde, W. W. Tjiu, Y. Cui and X. Y. Ling, *Small*, 2014, **10**, 4940–4950.

34 Y. Zhang, S. He, W. Guo, Y. Hu, J. Huang, J. R. Mulcahy and W. D. Wei, *Chem. Rev.*, 2018, **118**, 2927–2954.

35 J. Low, J. Yu, Q. Li and B. Cheng, *Phys. Chem. Chem. Phys.*, 2014, **16**, 1111–1120.

36 X. C. Ma, Y. Dai, L. Yu and B. B. Huang, *Light: Sci. Appl.*, 2016, **5**, e16017.

37 M. L. Brongersma, N. J. Halas and P. Nordlander, *Nat. Nanotechnol.*, 2015, **10**, 25–34.

38 J. Yang, Y. Guo, R. Jiang, F. Qin, H. Zhang, W. Lu, J. Wang and J. C. Yu, *J. Am. Chem. Soc.*, 2018, **140**, 8497–8508.

39 Z. Li, F. Zhang, A. Meng, C. Xie and J. Xing, *RSC Adv.*, 2015, **5**, 612–620.

40 S. J. Lv, Y. P. Du, F. T. Wu, Y. C. Cai and T. Zhou, *Nanoscale Adv.*, 2022, **4**, 2608–2631.

41 S. Karak, S. Kandambeth, B. P. Biswal, H. S. Sasmal, S. Kumar, P. Pachfule and R. Banerjee, *J. Am. Chem. Soc.*, 2017, **139**, 1856–1862.

42 T. Wu, Q. Zhang, Y. Hou, L. Wang, C. Mao, S. T. Zheng, X. Bu and P. Feng, *J. Am. Chem. Soc.*, 2013, **135**, 10250–10253.

43 Z. Wang, Y. Inoue, T. Hisatomi, R. Ishikawa, Q. Wang, T. Takata, S. Chen, N. Shibata, Y. Ikuhara and K. Domen, *Nat. Catal.*, 2018, **1**, 756–763.

44 K. M. Koczkur, S. Mourdikoudis, L. Polavarapu and S. E. Skrabalak, *Dalton Trans.*, 2015, **44**, 17883–17905.

45 Z. Xin, L. Li, X. Zhang and W. Zhang, *RSC Adv.*, 2018, **8**, 6027–6038.

46 S. Ghosh, R. A. Molla, U. Kayal, A. Bhaumik and S. M. Islam, *Dalton Trans.*, 2019, **48**, 4657–4666.

47 P. Dong, C. Meng, Y. Yan, B. Zhang, W. Wang, X. Xi and J. Zhang, *Int. J. Hydrogen Energy*, 2023, **48**, 18670–18684.

48 Q. Deng, H. Tang, G. Liu, X. Song, G. Xu, Q. Li, D. H. L. Ng and G. Wang, *Appl. Surf. Sci.*, 2015, **331**, 50–57.

49 K. L. Li, X. T. Ma, L. Wang, X. T. Yang, X. Z. Qu, S. Y. Zhou, B. C. Xu, S. He, G. J. Zhang and S. Y. Guan, *ACS Biomater. Sci. Eng.*, 2022, **8**, 540–550.

50 I. Vukoje, V. Lazic, D. Sredojevic, M. M. Fernandes, S. Lanceros-Mendez, S. P. Ahrenkiel and J. M. Nedeljkovic, *Int. J. Biol. Macromol.*, 2022, **194**, 461–469.

51 D. Masekela, N. C. Hintsho-Mbita, B. Ntsendwana and N. Mabuba, *ACS Omega*, 2022, **7**, 24329–24343.

52 M. Sayed, J. Yu, G. Liu and M. Jaroniec, *Chem. Rev.*, 2022, **122**, 10484–10537.

53 D. F. Swearer, H. Zhao, L. Zhou, C. Zhang, H. Robatjazi, J. M. P. Martirez, C. M. Krauter, S. Yazdi, M. J. McClain, E. Ringe, E. A. Carter, P. Nordlander and N. J. Halas, *Proc. Natl. Acad. Sci. U.S.A.*, 2016, **113**, 8916–8920.

54 K. Sugawa, N. Tsunenari, H. Takeda, S. Fujiwara, T. Akiyama, J. Honda, S. Igari, W. Inoue, K. Tokuda, N. Takeshima, Y. Watanuki, S. Tsukahara, K. Takase, T. Umegaki, Y. Kojima, N. Nishimiya, N. Fukuda, Y. Kusaka, H. Ushijima and J. Otsuki, *Langmuir*, 2017, **33**, 5685–5695.

55 H. Wang, W. D. Zhang, X. W. Li, J. Y. Li, W. L. Cen, Q. Y. Li and F. Dong, *Appl. Catal., B*, 2018, **225**, 218–227.

56 G. Y. Yao and Z. Y. Zhao, *J. Mater. Chem. C*, 2020, **8**, 8567–8578.

57 N. N. Jiang, X. L. Zhuo and J. F. Wang, *Chem. Rev.*, 2018, **118**, 3054–3099.

58 N. J. Halas, S. Lal, W. S. Chang, S. Link and P. Nordlander, *Chem. Rev.*, 2011, **111**, 3913–3961.

59 W. Y. Li, P. H. C. Camargo, X. M. Lu and Y. N. Xia, *Nano Lett.*, 2009, **9**, 485–490.

60 C. E. Talley, J. B. Jackson, C. Oubre, N. K. Grady, C. W. Hollars, S. M. Lane, T. R. Huser, P. Nordlander and N. J. Halas, *Nano Lett.*, 2005, **5**, 1569–1574.

61 Y. Kim, D. H. Wi, J. W. Hong and S. W. Han, *ACS Nano*, 2023, **17**, 18641–18651.

62 Z. Wang, D. Wang, F. Deng, X. Liu, X. Li, X. Luo, Y. Peng, J. Zhang, J. Zou, L. Ding and L. Zhang, *Chem. Eng. J.*, 2023, **463**, 142313.

63 X. H. Jiang, L. S. Zhang, H. Y. Liu, D. S. Wu, F. Y. Wu, L. Tian, L. L. Liu, J. P. Zou, S. L. Luo and B. B. Chen, *Angew. Chem., Int. Ed.*, 2020, **59**, 23112–23116.

64 S. Fang, X. Zhu, X. Liu, J. Gu, W. Liu, D. Wang, W. Zhang, Y. Lin, J. Lu, S. Wei, Y. Li and T. Yao, *Nat. Commun.*, 2020, **11**, 1029.

65 M. J. Yang, Y. Zhang, J. H. Jian, L. Fang, J. Li, Z. S. Fang, Z. K. Yuan, L. M. Dai, X. D. Chen and D. S. Yu, *Angew. Chem., Int. Ed.*, 2019, **58**, 16217–16222.

66 Z. H. Pu, I. S. Amiinu, Z. K. Kou, W. Q. Li and S. C. Mu, *Angew. Chem., Int. Ed.*, 2017, **56**, 11559–11564.

67 Y. Zheng, Y. Jiao, Y. H. Zhu, L. H. Li, Y. Han, Y. Chen, A. J. Du, M. Jaroniec and S. Z. Qiao, *Nat. Commun.*, 2014, **5**, 3783.

68 Q. Zhao, J. Sun, S. C. Li, C. P. Huang, W. F. Yao, W. Chen, T. Zeng, Q. Wu and Q. J. Xu, *ACS Catal.*, 2018, **8**, 11863–11874.

69 X. She, H. Xu, Y. Yu, L. Li, X. Zhu, Z. Mo, Y. Song, J. Wu, S. Yuan and H. Li, *Small*, 2019, **15**, 201804613.

70 X. She, H. Xu, Y. Yu, L. Li, X. Zhu, Z. Mo, Y. Song, J. Wu, S. Yuan and H. Li, *Small*, 2019, **15**, e1804613.

71 A. Gellé, T. Jin, L. de la Garza, G. D. Price, L. V. Besteiro and A. Moores, *Chem. Rev.*, 2020, **120**, 986–1041.

72 Y. C. Zhang, S. He, W. X. Guo, Y. Hu, J. W. Huang, J. R. Mulcahy and W. D. Wei, *Chem. Rev.*, 2018, **118**, 2927–2954.

73 H. B. Michaelson, *J. Appl. Phys.*, 1977, **48**, 4729–4733.

74 S. Bai, X. Li, Q. Kong, R. Long, C. Wang, J. Jiang and Y. Xiong, *Adv. Mater.*, 2015, **27**, 3444–3452.

This journal is © The Royal Society of Chemistry 2024

J. Mater. Chem. A, 2024, **12**, 5392–5405 | **5405**